The Astrophysical Journal, 863:43 (12pp), 2018 August 10 https://doi.org/10.3847/1538-4357/aacb34

The X-Ray Luminosity Function of Ultraluminous X-Ray Sources in Collisional Ring Galaxies

Anna Wolter[1], Antonella Fruscione[2], and Michela Mapelli[3]
[1] INAF-Osservatorio Astronomico di Brera, via Brera 28, I-20121 Milano, Italy
[2] Harvard-Smithsonian Center for Astrophysics, 60 Garden St., Cambridge, MA, 02138, USA
[3] INAF-Osservatorio Astronomico di Padova, vicolo dell'Osservatorio 5, I-35122, Padova, Italy
Received 2018 March 7; revised 2018 June 4; accepted 2018 June 5; published 2018 August 8

Abstract

Ring galaxies are fascinating laboratories: a catastrophic impact between two galaxies (one not much smaller than the other) has produced fireworks, especially in the larger one, when hit roughly perpendicularly to the plane. We analyze the point sources produced by the starburst episode following the impact in the rings of seven galaxies and determine their X-ray luminosity function (XLF). In total, we detect 63 sources, of which 50 have luminosity $L_X \geqslant 10^{39}$ erg s^{-1}, classifying them as ultraluminous X-ray sources (ULXs). We find that the total XLF is not significantly different from XLFs derived for other kinds of galaxies, with a tendency of having a larger fraction of high X-ray luminosity objects. Both the total number of ULXs and the number of ULXs per unit star formation rate are found in the upper envelope of the more normal galaxies distribution. Further analysis would be needed to address the issue of the nature of the compact component in the binary system.

Key words: galaxies: individual (AM 0644-741, Arp 143, Arp 148) – galaxies: peculiar – galaxies: star formation – X-rays: binaries

1. Introduction

Ring Galaxies (RiGs) are unique laboratories in which to study peculiar phases of galaxy evolution. At least a fraction of RiGs are thought to form via (almost) head-on collisions with massive intruder galaxies. Due to the gravitational perturbation induced by the bullet galaxy, a density wave propagates through the disc of the target galaxy, generating an expanding ring of gas and stars (e.g., Lynds & Toomre 1976). They are often characterized by high star formation rates (SFR $\approx$ 0.1–20 $M_\odot$ yr^{-1}), suggesting that the density wave associated with the propagating ring triggers the formation of stars. Even if they constitute a small subclass of galaxies (they are estimated to be about 0.02%–0.2% of all spiral galaxies, Athanassoula & Bosma 1985), they represent a peculiar and energetic environment worth investigating.

The RiG archetype is the Cartwheel galaxy (see e.g., Wolter et al. 1999; Wolter & Trinchieri 2004 for a description of the X-ray emission in the Cartwheel and references for multi-wavelength observations). It is bright in all bands and contains a large number of ultraluminous X-ray sources (ULXs), most of which trace the star-forming regions in the ring.

ULXs are off-center, point-like sources with X-ray luminosity (assumed isotropic) $L_X > 10^{39}$ erg s^{-1}, higher than the Eddington limit for a few $M_\odot$ black hole (BH). The general consensus until recently was that most ULXs represent the high-luminosity tail of high-mass X-ray binaries (HMXBs; see, for instance, the X-ray luminosity functions (XLFs) of ULX in the Cartwheel, Antennae, and NGC 2276 in Wolter & Trinchieri 2004; Zezas et al. 2007; Wolter et al. 2015), and the BHs powering them are of (heavy) stellar-mass size (Feng & Soria 2011; Kaaret et al. 2017). However, it has not yet been excluded that a number of ULXs are powered by intermediate-mass black holes (IMBH). IMBHs are compact objects with masses in the range 10^2–10^5 $M_\odot$, which are intermediate between stellar-mass BHs and super-massive BHs in the center of galaxies (see e.g., van der Marel 2004, for a review), and have fundamental cosmological implications, as they are deemed to be seeds of super-massive BHs, sources of pre-heating of the intergalactic medium (e.g., Fragos et al. 2013; Mesinger et al. 2013), of fluctuations in the near-infrared cosmic background (Yue et al. 2013) and of gravitational waves (e.g., Mapelli 2016; Abbott et al. 2017c). Furthermore, recent observations have found that at least four ULXs, including one of the most luminous, are powered by a neutron star (NS), betraying its presence through X-ray pulsations, hence the name PULXs, from pulsar ULXs (Bachetti et al. 2014; Fürst et al. 2016; Israel et al. 2017a, 2017b; Carpano et al. 2018). Indeed, it might even turn out that all ULXs are NS (e.g., King & Lasota 2016).

It is therefore most likely that the class of ULXs, being defined purely on one single observational parameter (their X-ray luminosity), contains a mixed class of sources. Mass measure is a very challenging task for ULXs, and only few reliable results are available. The dynamical evidence for a small mass for the compact object is scant: it comes mostly from ULX-1 in M101 (Liu et al. 2013), and P13 in NGC 7793 (Motch et al. 2014). In fact, source P13 turned out to be a NS (Israel et al. 2017b; Walton et al. 2018). On the other hand, the most luminous ULXs known, and therefore the most promising IMBH candidates, are M82-X1 (Portegies Zwart et al. 2004; Feng et al. 2010), ESO 243-49 HLX-1 (Farrell et al. 2009), NGC 2276-S6, (Mezcua et al. 2015), and Cartwheel-N10 (Wolter et al. 2006).

With the aim of studying ULXs of extreme properties in extreme environments, we decided to better investigate a sample of RiGs in search for ULXs. The objects in our sample are similar to the Cartwheel, suggesting the presence of a catastrophic event. If RiGs are "caught in the act" of forming new stars, we might be in a better position for finding the most massive products of star formation. Ages of rings are estimated to be of not longer than a few hundred Myr (see Section 2.1 for age determinations, when available, and references). Furthermore, due to the peculiar morphology of ring galaxies, point

Table 1
Observed Ring Galaxies

Name (Other Name)	Position J2000		N_H (10^{20} cm^{-2})	Dist (Mpc)	Diam (′)	Scale (kpc/(″))
Cartwheel Galaxy (AM 0035−335)	00 37 41.1	−33 42 59	19.0	122	1.5	0.566
NGC 922 (AM 0222−250)	02 25 04.4	−24 47 17	1.62	48	2.6	0.239
Arp 147	03 11 18.9	+01 18 53	6.2	133	0.5	0.643
AM 0644−741 (Lindsay-Shapley Ring)	06 43 06.1	−74 13 35	10.0	91.6	1.7	0.447
Arp 143	07 46 53.6	+39 01 10	5.01	57.1	3.0	0.283
Arp 148 (Mayall's object)	11 03 53.2	+40 50 57	1.01	145.2	0.6	0.696
Arp 284 (NGC 7714/7715)	23 36 18.1	+02 09 21	18.0	37	2.9	0.186

Note. Data are from NED unless specified otherwise; N_H and distance from literature as in Table 3; scale is the plate scale at the galaxies' distance.

Table 2
Galaxy Properties from the Literature

Name	M_K	B	SFR ($M_\odot$ yr^{-1})	Z[a] ($Z_\odot$)	References[b] (SFR, Z)
Cartwheel		14.82[c]	20	0.14	1, 2
NGC 922	−23.21	12.32	8.0	0.5-1.	3, 3
Arp 147	−22.88	15.99 ± 0.05	4.1	0.19–0.40	4, 5
AM 0644−741		11.0 ± 0.4	2.6	0.45	6, 7
Arp 143	−23.86	13.30 ± 0.08	2.3	0.44–0.71	4, 8
Arp 148	−23.23	16.04 ± 0.03	2.5		4, –
Arp 284			4.0	0.19–0.38	9, 10

Notes. M_K and B are from NED, SFR and Z from References in column 6.
[a] Assuming $Z_\odot = 0.02$, $12+\log(O/H)_\odot = 8.92$.
[b] Reference list: 1: H_α data: Appleton & Marston (1997), 2: Fosbury & Hawarden (1977), 3: H_α data Wong et al. (2006), 4: H_α data: Romano et al. (2008), 5: from $\log(NII/H_\alpha)$ in different ring positions (Fogarty et al. 2011); 6: H_α data Higdon & Wallin (1997), 7: Mapelli et al. (2009), 8: Higdon et al. (1997) citing Jeske (1986), 9: H_α data Schmitt et al. (2006), 10: García-Vargas et al. (1997).
[c] B-Magnitude of the ring.

sources detected in the ring are very likely to be physically associated with the galaxy, reducing the problem of contamination from spurious sources.

We collected therefore all seven collisional RiGs observed by *Chandra*, three of which analyzed for the first time in this paper, with the aim of constructing their global XLF to study the population of ULXs on statistical grounds. Section 2 describes the sample and the individual galaxies; Section 3 the XLF; and Section 4 our discussion of the findings. We use $H_0 = 73$ Km s^{-1} Mpc^{-1} to compute X-ray luminosities.

2. The Sample

Collisionally formed rings, with enhanced star formation, represent an ideal nursery to collect a fair sample of ULXs. Yet, only a few X-ray observations of ring galaxies exist. We focus on the objects observed by the *Chandra* satellite because of the superior spatial resolution of the telescope, that allows for a better identification of the sources and less source confusion.

Chandra observed only seven RiGs, but they make up for this paucity by having a large number of individual sources. These galaxies were selected for observation because they are bright and have a spectacular morphology in all known wavebands. Of the seven galaxies, four have been published already in the literature. The X-ray observations of the remaining three galaxies are unpublished, except that in one case the literature reports only the identification of the brightest source with an interloper AGN. We have analyzed their *Chandra* data, and list here the relevant findings for point sources (see Section 2.1). To construct the XLF we will consider only sources along the ring. Below we list and describe all the RiGs considered in this paper.

2.1. Individual Galaxies

Table 1 lists the relevant information for all the galaxies: name, position, Galactic line-of-sight absorption (N_H) as used in this paper, distance in Mpc as used in this paper, optical diameter (D25 from the NASA/IPAC Extragalactic Database —NED), and the scale at the distances of the galaxies. We describe below each galaxy in turn, concentrating mainly on the references and information about the X-ray analysis, the star formation rate (SFR), and the metallicity of the galaxies. We use as the primary SFR indicator the Hα derived value, which is most sensitive to the recent star formation. We expect the stellar population to be of young age (see below). This is also favoring the presence of massive OB stars as donors, as is the case for HMXB, although the issue is far from settled, as a few ULXs may have a late star as optical counterpart (e.g., IC 342 X1: Feng & Kaaret 2008) and main-sequence stars are favored as donors in simulations, due to their longer life (e.g., Wiktorowicz et al. 2017). Where available, we report other SFRs from the literature. We list in Table 2 all of the relevant properties from the literature: absolute K magnitude and B mag from NED, SFR (as used in this paper), and Z (as used in this paper) from the references listed.

2.1.1. Cartwheel Galaxy (AM 0035–335)

The Cartwheel is the most famous object in the group. It has been studied extensively at all wavelengths. Several authors have studied this galaxy in great detail, both in the X-ray and other wavebands (e.g., Wolter et al. 1999, 2006; Gao et al. 2003; Wolter & Trinchieri 2004; Crivellari et al. 2009; Pizzolato et al. 2010 for the description of the X-ray data). The Cartwheel contains 16 ULX (Wolter & Trinchieri 2004) and has a high SFR; Wolter & Trinchieri (2004) find it consistent with the SFR $\sim 20\,M_{\odot}\,\mathrm{yr}^{-1}$ obtained from $L_{\mathrm{H}\alpha}$ (Appleton & Marston 1997), while Mayya et al. (2005) derive a SFR $= 18\,M_{\odot}\,\mathrm{yr}^{-1}$ from radio data. The metallicity has been measured by Fosbury & Hawarden (1977) at the position of the brightest H II regions in the ring, and the result is sub-solar: $Z = 0.14\ Z_{\odot}$, assuming $Z_{\odot} = 0.019$ (Anders & Grevesse 1989).

The nuclear mass of the Cartwheel, derived from the rotation velocity in the ring, is $M = 4 \times 10^{11}\ M_{\odot}$, while the ring contains stars and ionized gas for a total of $M_{\mathrm{star}} \sim 2 \times 10^{10}\ M_{\odot}$ and $M_{\mathrm{gas}} \geqslant 1.2 \times 10^{8}\ M_{\odot}$ (Fosbury & Hawarden 1977).

CO is detected by ALMA only in the nucleus and inner ring (Higdon et al. 2015) for a total mass of $2.7 \times 10^{9}\ M_{\odot}$. The kinematic of the gas implies an age of the inner ring of ~70 Myr. The outer ring appears dominated by an atomic phase of the gas, with a very little content of H_2. The age of the outer ring is estimated to be ~440 Myr (Higdon 1995, 1996).

In this paper, we use the results of the X-ray analysis as presented in Wolter & Trinchieri (2004).

2.1.2. NGC 922 (AM 0222–250)

NGC 922 has been described as a RiG only recently (Wong et al. 2006). It contains 7 ULXs and has a SFR $= 8\,M_{\odot}\,\mathrm{yr}^{-1}$ (Wong et al. 2006; Prestwich et al. 2012) derived from H_{α} measures, which we use hereafter.

The ring has a distorted appearance that probably hindered the classification of the galaxy. However, the high SFR and high number of ULXs are consistent with it being a collisional RiG. Metallicity has been published only for the nucleus of the galaxy (Wong et al. 2006), and is consistent with solar (following Prestwich et al. 2012, we adopt $Z \sim 0.75\ Z_{\odot}$). Optical spectra taken at optical knots positions suggest a smaller value for metallicity in the ring (E. Ripamonti 2015, private communication). The gravitational interaction of the bullet galaxy (S2) with NGC 922 has likely happened about 330 Myr ago (Wong et al. 2006) with a slightly off-center impact. Pellerin et al. (2010) find young stellar clusters in the ring and nuclear region, while the plume is made of older stars, consistent with the impact scheme.

In this paper, we use the results of the X-ray analysis as presented in Prestwich et al. (2012).

2.1.3. Arp 147

Arp 147 lives in one of the most diverse collections of celestial objects in a small patch of the sky: in the close vicinity of the RiGs, there are the possible intruder galaxy, a bright star, and an X-ray emitting AGN. All within less than 1′. Rappaport et al. (2010) have analyzed this galaxy and list 9 ULXs and a SFR of $7\,M_{\odot}\,\mathrm{yr}^{-1}$.

A SFR of $4.1\,M_{\odot}\,\mathrm{yr}^{-1}$ from Hα and of $8.6\,M_{\odot}\,\mathrm{yr}^{-1}$ from FIR is derived by Romano et al. (2008). We use the Hα derived value. Metallicity has been measured via the N2 ratio defined as $\mathrm{N2} = \log(\mathrm{N\,II}/\mathrm{H}_{\alpha})$ in different ring quadrants and ranges between $Z = 0.19$–$0.40\ Z_{\odot}$ (Fogarty et al. 2011).

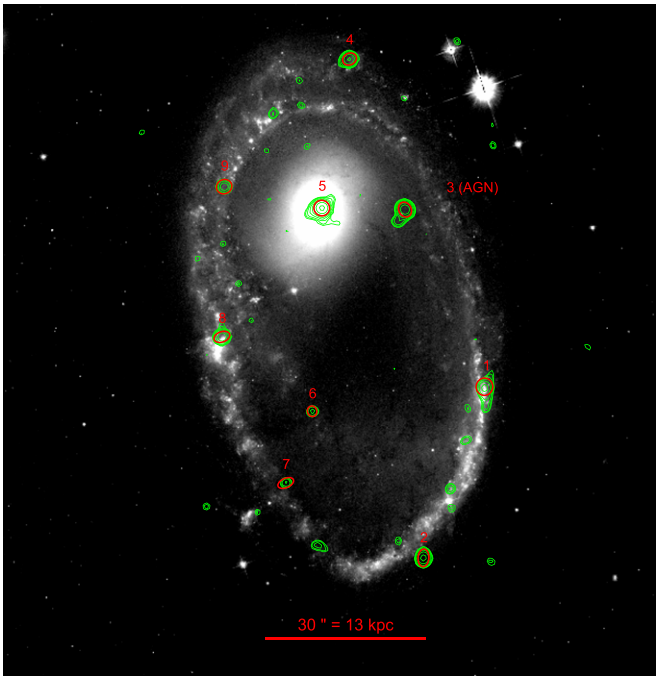

Figure 1. AM 0644-741. *Hubble Space Telescope* (*HST*) ACS WFC1 F555W image and superimposed the detected X-ray sources (in red) and X-ray contours (in green) from *Chandra* data. The scale of the figure is given in the red bar.

Less than ~50–80 Myr have elapsed since the collision, as indicated by *N*-body simulations (Gerber et al. 1996; Mapelli & Mayer 2012). In this paper, we use the results of the X-ray analysis as presented in Rappaport et al. (2010).

2.1.4. AM 0644-741 (Lindsay-Shapley Ring)

AM 0644-741 (see Figure 1) shows an almost complete ring, and a partial second, more internal ring. It is probably the galaxy most similar to the Cartwheel in morphology, except for the presence of an active nuclear source.

The brightest source in AM 0644-741(#3) has been observed spectroscopically by Heida et al. (2013), and it has been identified with an AGN at $z = 1.40$. The source is not positionally coincident with the ring, and therefore it does not belong to the sample which we use for the XLF.

In this paper, we use a SFR of $2.6\,M_{\odot}\,\mathrm{yr}^{-1}$ derived from Hα by Higdon & Wallin (1997) and sub-solar metallicity of $Z = 0.45\ _{\odot}$ (Mapelli et al. 2009). However, we are aware that Higdon et al. (2011) derive a SFR $= 11.2 \pm 0.4\,M_{\odot}\,\mathrm{yr}^{-1}$ from $L_{\mathrm{H}\alpha}$ and the less favored SFR $= 17.6 \pm 0.9\ M_{\odot}\ \mathrm{yr}^{-1}$ from radio measures, in addition to a metallicity in excess of solar with no significant azimuthal variations.

The *Chandra* X-ray observation is not published, so we downloaded it from the archive and analyzed it as described below (see Section 2.2). All nine detected point sources are listed in Table 4. Their luminosities are all above the ULX limit if associated to the galaxy. The list includes one source associated to the nucleus. In addition to #3, we will exclude this source from the XLF computation.

From the total detected net counts in the area of the galaxy (excluding the interloper AGN and the nuclear source) of 593.0 ± 37.0, we measure a total unabsorbed luminosity associated with the galaxy of L_{X} (0.5–10 keV) $= 1.78 \times 10^{41}\ \mathrm{erg\ s}^{-1}$. We

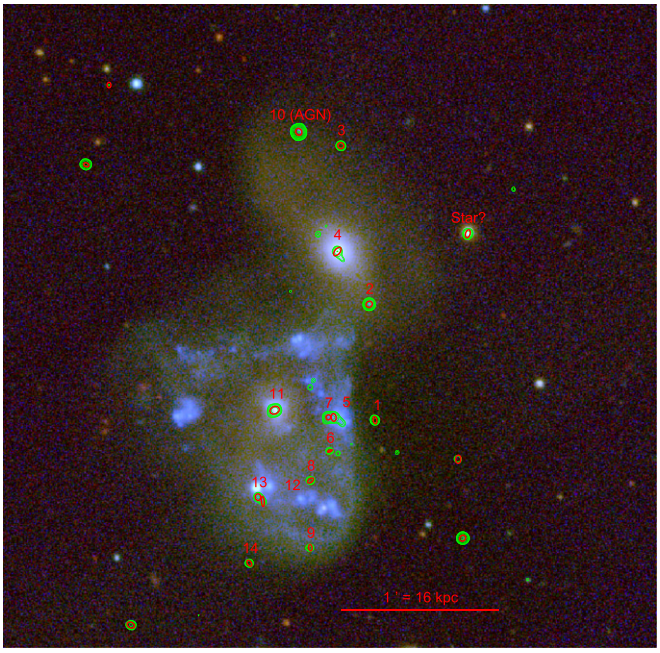

Figure 2. Arp 143. SDSS-III image (RGB representation with SDSS bands z, g, u, respectively) and superimposed the detected X-ray sources (in red) and X-ray contours (in green) from *Chandra* data. The six sources outside the boundaries of the galaxy pair were not considered in this paper. The scale of the figure is given in the red bar.

assumed a spectral shape that includes both a "point sources" spectrum with fixed $\Gamma = 1.7$ and a thermal plasma (*mekal* in XSPEC) component to describe the diffuse gas, both absorbed by a fixed $N_{\rm H} = 0.1 \times 10^{22}$ cm^{-2}. The fraction accounted for by the thermal component corresponds to an unabsorbed $L_{\rm X}$ (0.5–10 keV) $= 9.74 \times 10^{39}$ erg s^{-1} with $kT = 0.08$ (<0.33) keV. We extracted the counts for all detected point sources (178.1 counts in total) and derived a mean spectral shape of $N_{\rm H} = 0.22$ [0.01–0.43] $\times 10^{22}$ cm^{-2} and $\Gamma =$ 1.55 [1.18–1.99] for a total unabsorbed $L_{\rm X}$ (0.5–10 keV) $=$ 2.6×10^{40} erg s^{-1}. Most of the X-ray luminosity is in unresolved sources.

2.1.5. Arp 143

Arp 143 (see Figure 2) has a complex morphology. It consists of the galaxies NGC 2444 and NGC 2445. The Galex image clearly shows the young stellar population in the ring (Beirão et al. 2009). H I and CO are detected in the galaxy: H I in the ring and CO clustered around the nucleus (Higdon et al. 1997), together with a number of H II regions. A long (∼100 kpc) H I tail (Appleton et al. 1987) might represent the leftover of previous, perhaps multiple encounters. The kinematics of the ring implies an age of the ring of 60 ± 15 Myr, about 20% of the Cartwheel, and the *N*-body simulations of Gerber et al. (1996) imply that time elapsed since the collision is less than 80 Myr. About 30 Myr have elapsed since the encounter, assuming NGC 2444 is the bullet galaxy and based on the dynamics and distance of the two galaxies (from Jeske 1986 referred to in Higdon 1995). The total molecular gas content is estimated to be $H_2 = (4–24) \times 10^9 M_\odot$ (Higdon 1995).

Romano et al. (2008) find a SFR $= 2.30\, M_\odot\, {\rm yr}^{-1}$ from H_α and a SFR $= 5.6\, M_\odot\, {\rm yr}^{-1}$ from FIR. We use the H_α derived SFR and a sub-solar metallicity from Jeske (1986), cited by Higdon et al. (1997) as $Z = 0.44–0.71\ Z_\odot$.

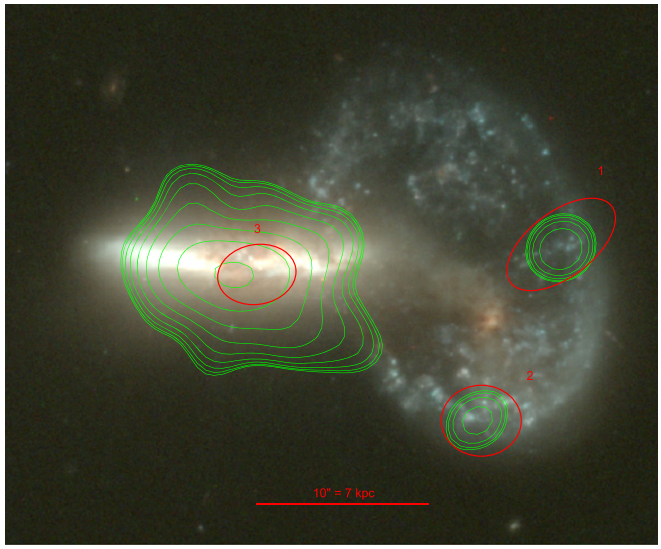

Figure 3. Arp 148. *Hubble* Heritage image (WFP2 F814W/F555W/F450W) and superimposed the detected X-ray sources (in red) and X-ray contours (in green) from *Chandra* data. The scale of the figure is given in the red bar.

The *Chandra* X-ray observation is not published, so we downloaded it from the archive and analyzed it as described below (see Section 2.2). All 14 detected point sources are listed in Table 4. Both nuclei are detected in the galaxies forming Arp 143, plus an interloper Sy1 at $z = 0.6155313$ (Abolfathi et al. 2018). Two sources have a radio counterpart including the nucleus of NGC 2445. A couple more of X-ray sources (noted in Table 4) are not consistent with the ring position and will not be used to derive the XLF.

From the total detected net counts in the area of the galaxy (excluding the Sy1 and the two nuclear sources) of 490.6 ± 39.6, we measure a total unabsorbed luminosity associated with the galaxy of $L_{\rm X}$ (0.5–10 keV) $= 4.81 \times 10^{40}$ erg s^{-1}. We assumed a spectral shape with fixed $N_{\rm H} = 0.05 \times 10^{22}$ cm^{-2} that includes a point sources spectrum with fixed $\Gamma = 1.7$ and a thermal plasma (*mekal* in XSPEC) component to describe the diffuse gas. The fraction accounted for by the thermal component corresponds to an unabsorbed $L_{\rm X}$ (0.5–10 keV) $=$ 7.99×10^{39} erg s^{-1} with $kT = 0.50$ (0.32–0.66) keV. We extracted the counts for all detected point sources (247.1 counts in total) and derived a mean spectral shape of $N_{\rm H} =$ 0.074 [<0.187] $\times 10^{22}$ cm^{-2} and $\Gamma = 1.57$ [1.26–1.94] for a total unabsorbed $L_{\rm X}$ (0.5–10 keV) $= 2.6 \times 10^{40}$ erg s^{-1}.

2.1.6. Arp 148 (Mayall's Object)

Arp 148 (see Figure 3) is a beautiful example of an interacting pair. We detect only two sources in the ring, beside the foreground member of the pair, which is also a radio source. However, the limiting flux of the *Chandra* observation corresponds to much higher luminosity of $L_{\rm X} = 5 \times 10^{39}$ erg s^{-1} than the other galaxies, given the much larger distance and comparatively short exposure time.

The galaxy lies in fact at $D = 145$ Mpc (Strauss et al. 1992) with a low galactic line-of-sight absorption of $N_{\rm H} = 1.04 \times 10^{20}$ cm^{-2}. The source was observed by *Chandra* on 2011 February 7 for a total of 52.34 ks. The X-ray observation is not

published so we downloaded it from the archive and analyzed it as described below (see Section 2.2). All the detected point sources are listed in Table 4. In our analysis, we used a SFR = $2.5\,M_{\odot}\,\mathrm{yr}^{-1}$ from H_{α} (Romano et al. 2008). A SFR = $65.06\,M_{\odot}\,\mathrm{yr}^{-1}$ is derived from the far-infrared (Romano et al. 2008); however, given the low resolution of the IRAS data, this measurement could be affected by confusion due to the presence of the companion galaxy, which could host an AGN, being a radio emitter. The metallicity is not known. Romano et al. (2008) estimate an elapsed time since collision of less than 80 Myr, based on *N*-body simulations of Gerber et al. (1996).

The total unabsorbed luminosity associated with the ring galaxy, computed with a spectral shape with fixed $N_{\mathrm{H}} = 0.01 \times 10^{22}\ \mathrm{cm}^{-2}$ that includes a point sources spectrum with fixed $\Gamma = 1.7$ and a thermal plasma (*mekal* in XSPEC) component to describe the diffuse gas, is of L_{X} (0.5–10 keV) = $3.87 \times 10^{41}\ \mathrm{erg\,s}^{-1}$ given the total detected net counts in the area of the ring galaxy (excluding the interloper) of 73.6 ± 13.3. The fraction accounted for by the thermal component corresponds to an unabsorbed L_{X} (0.5–10 keV) = $1.28 \times 10^{41}\ \mathrm{erg\,s}^{-1}$ with $kT = 0.23$ (0.17–0.31) keV. However, the small number of counts does not allow a very reliable fit. As a last step, we extracted the counts for all detected point sources (34.0 counts in total) and derived a mean spectral shape of $N_{\mathrm{H}}^{\mathrm{fixed}} = 0.01 \times 10^{22}\ \mathrm{cm}^{-2}$ and $\Gamma = 1.63$ [1.14–2.14] for a total unabsorbed luminosity L_{X} (0.5–10 keV) = $1.5 \times 10^{40}\ \mathrm{erg\,s}^{-1}$.

Regarding the intruder galaxy, it is detected with total net counts = 384.0 ± 20.9. We fit the extracted spectrum with a power law to represent both the nucleus and possible unresolved point sources, plus a thermal plasma (*mekal* in XSPEC) component to account for the diffuse plasma. Both components are necessary to the fit. We fix the absorbing hydrogen column density to the Galactic value of $N_{\mathrm{H}} = 0.01 \times 10^{22}\ \mathrm{cm}^{-2}$. The resulting $\Gamma = 1.63$ [1.25–1.96] is perfectly consistent with both unresolved point sources or the presence of a nucleus, while the $kT = 0.66$ [0.58–0.74] keV is also similar to temperatures found for the gas in the other RiGs and for local galaxies in general (Bogdán & Gilfanov 2011). The unabsorbed flux is f_{X} (0.5–10 keV) = $5.02 \times 10^{-14}\ \mathrm{erg\,cm^2\,s}^{-1}$ for a luminosity L_{X} (0.5–10 keV) = $1.39 \times 10^{41}\ \mathrm{erg\,s}^{-1}$ where the two components contribute as follows: the power law L_{X} (0.5–10 keV) = $9.84 \times 10^{40}\ \mathrm{erg\,s}^{-1}$ and the diffuse gas L_{X} (0.5–10 keV) = $4.08 \times 10^{40}\ \mathrm{erg\,s}^{-1}$.

2.1.7. Arp 284 (NGC 7714/7715)

Arp 284 is the interacting pair NGC 7714 and NGC 7715, with many structures, for instance bridges between the two galaxies and tails. The galaxy contains 9 ULXs and has a SFR = $7\,M_{\odot}\,\mathrm{yr}^{-1}$ (Smith et al. 2005). While Lançon et al. (2001) find a SFR $\sim 1\,M_{\odot}\,\mathrm{yr}^{-1}$ from complex SED modeling, Schmitt et al. (2006) find a value of SFR = $4.0\,M_{\odot}\,\mathrm{yr}^{-1}$ from Hα data and a SED correction. We use this last Hα derived value. The metallicity has been measured by García-Vargas et al. (1997) to be $Z = 0.19$–$0.38\ Z_{\odot}$. We use only the sources in the ring, as listed in Table 5, to construct the XLF.

In this paper, we use the results of the X-ray analysis as presented in Smith et al. (2005).

2.2. Data Analysis

Chandra observations for all RiGs were performed with the Advanced CCD Imaging Spectrometer S Array (ACIS-S; Garmire et al. 2003), and their log is reported in Table 3. For each source, we list the observation Id (ObsID), the date of the observation, together with the total live time and the references for the published data for four of the galaxies. We refer to the original papers for a detailed description of the data analysis. Three of the galaxies are presented here for the first time (see Section 2.1 and Table 4). The ACIS detector was operated in the standard timed exposure full-frame mode, with FAINT (Arp 143) or VERY FAINT telemetry format. In all cases, the targets were positioned on the back-illuminated chip S3 (CCD7). The data were reprocessed with the *Chandra* Interactive Analysis of Observations software package (CIAO, version 4.7 and 4.8, Fruscione et al. 2006) and CALDB version[4] 4.6/4.7 (we note here that no significant changes have occurred in CIAO or the CALDB that could affect our analysis). We followed standard data reduction and analysis procedures. After downloading the data from the public archive, we run the CHANDRA_REPRO tool to perform all the recommended data processing steps, then the FLUXIMAGE tool to generate exposure-corrected images. Source detection was performed with the WAVEDETECT tool on an image of the S3 chip generated by FLUXIMAGE in the "broad" energy range (0.5–7 keV) after excluding low-exposure regions at the edge of the chips (the EXPMAPTHRESH parameter in FLUXIMAGE). The detected sources are visible in Figures 1–3 as positional error ellipses. We computed count rates and fluxes for all the detected sources using the SRCFLUX tool and assuming a power-law model with photon index $\Gamma = 1.7$ absorbed by an Hydrogen column density of N_{H} as listed in Table 1 for each galaxy. This choice is appropriate for ULXs (e.g., Swartz et al. 2011), which are unresolved at the *Chandra* resolution. The instrumental responses (ARF and RMF) were calculated for each source, while the PSF contribution to both the source and background regions was calculated with the ARFCORR method (where a simulated circularly symmetric PSF is used to estimate the aperture correction). Fluxes were calculated in the 0.5–10 keV and 2–10 keV energy bands for all the sources and are listed in Table 4. Luminosities were calculated assuming the galaxy distance from Table 1. The "XLF Corr" column contains the correction factors for each source as described in Section 3

In Figures 1–3, we display the optical image of the galaxies AM 0644-741, Arp 143, and Arp 148 and overplot the detected sources and X-ray contours from *Chandra* data. The description of the main results for each galaxy is in Section 2.1

Table 5 lists all the sources from the literature. For sake of uniformity and with the aim of constructing the X-ray luminosity function, we recalculated luminosities in the 0.5–10 keV band for all the ring sources from the literature. In all cases, we assumed the published N_{H} and a power-law model with photon index $\Gamma = 1.7$.

3. X-Ray Luminosity Function

To study the ULXs as a class and to be able to compare the results with different models and with results from different samples, we construct the XLF by incorporating the sources

[4] http://cxc.harvard.edu/ciao/

Table 3
Journal of *Chandra* Observations

Name	ObsID	Date	Time ($\times 10^3$ s)	References for X-Rays
Cartwheel Galaxy	2019	2001 May 26	76.15	Wolter & Trinchieri (2004)
NGC 922	10563	2009 Mar 05	29.74	Prestwich et al. (2012)
NGC 922	10564	2009 Oct 02	10.02	⋯
Arp 147	11280	2009 Sep 13	24.53	Rappaport et al. (2010)
Arp 147	11887	2009 Sep 15	18.04	⋯
AM 0644−741	3969	2003 Nov 17	39.40	this paper
Arp 143	14906	2012 Dec 10	39.00	this paper
Arp 148	12977	2011 Feb 07	52.34	this paper
Arp 284	4800	2004 Jan 24	59.00	Smith et al. (2005)

detected in all the rings. The purpose is to see if an encounter as violent as the splashdown of a bullet galaxy into another galaxy is so energetic as to create a different "flavor" of ULXs, or a different distribution in luminosity. RiGs might host the most extreme class of ULXs. We assume that the ring population represents a single burst of star formation, produced by the impact, and that the populations from the different galaxies are homogeneous and can be combined. Luminosities are taken from Tables 4 and 5 and recalculated in the (0.5–10) keV band for uniformity with previous studies. We have collected a total of 63 sources, of which 50 above the ULX limit (10^{39} erg s^{-1}). There are 23 sources with $L_X > 5 \times 10^{39}$ erg s^{-1} and 8 with $L_X > 1 \times 10^{40}$ erg s^{-1}.

To take into account the detection confusion due the presence of diffuse and unresolved emission linked to the galaxies, we have applied a correction to the efficiency of detection following Kim & Fabbiano (2003). We base our assessment on Figure 12 from Kim & Fabbiano (2003) in which the detection probabilities as a function of background counts and source counts are plotted. The background includes both diffuse emission from the galaxy and field background and is estimated for each galaxy by averaging the total counts in the ring region, after excluding detected sources. We use the second panel, relative to a 2 arcmin off-axis, since the galaxies are always entirely within this limit. We apply the interpolated correction—listed in Tables 4 and 5—to all sources with less than 22 counts. This represents a conservative estimate.

We assess the probability of interlopers by measuring the number of sources expected by chance in the area of the rings in which we run the detection algorithm. We conservatively use an elliptical annulus that includes all of the optical extent of the ring. The density of sources at the limiting fluxes for each galaxy is derived from Moretti et al. (2003). As the Log N–log S is given in the (0.5–2 keV) band, we used the 0.5–2 keV flux limit for each field (computed along the galaxies' ring) derived with the same spectral hypothesis. The total expected number of interlopers is <1 for each galaxy at the relative detection limit and in total it is ∼1.1. Given these numbers, we disregard the interlopers and remove no further sources from the XLF.

We plot the resulting XLF in Figure 4 for each galaxy and in Figure 5 for the sum of all sources, distinguishing sources from the same host galaxy by the same color and symbol. We notice that as not all observations have the same limiting luminosity, the sampling at low L_X is still not complete, even after the correction for the higher background due to the galaxy contribution. This explains the flattening below $L_X \sim 10^{39}$ erg s^{-1}; because we are interested mainly in the high-luminosity end of the XLF, we do not consider this fact as a major problem at this time.

We have considered also two potential observational biases that could affect the final XLF. First, high absorbing columns of gas within the galaxies could obscure ULXs and lead to an underestimate of their numbers. For instance, Luangtip et al. (2015) find that the high absorbing columns of 10^{22}–10^{24} cm^{-2} and dust content in luminous infrared galaxies might be a cause for the smaller number of ULXs per SFR unit they found. However, in RiGs, the absorbing columns due to our Galaxy are in the 10^{21} cm^{-2} range at most, and fitted values in the ULX spectra (when statistics allows to perform a fit) are about at the same 10^{21} cm^{-2} level. Furthermore, the effect of a high absorbing column would be stronger for lower-luminosity sources. We have sufficiently low detection limits, except for the case or Arp 148, that this should not be a problem. The most significant cause for losing low flux sources would be the enhanced background due to the diffuse galactic emission, which we corrected for. Second, the finite angular resolution may cause multiple sources to be detected as a single one, with an artificially higher luminosity, with the effect of flattening the high-luminosity end of the XLF. If we take the Cartwheel as a reference, we know that most of ULXs are variable (Wolter et al. 2006; Crivellari et al. 2009), and therefore more likely to be single sources. A higher X-ray spatial resolution could indeed resolve a few ULXs. With the statistics in hand, however, we do not find any difference in the high L_X end of the XLF by dividing the sample in near and far galaxies (most likely to be unresolved). The statistics however is not large, therefore more numerous samples are needed to estimate if the effect is present at low levels.

We compare our results with previous work on XLFs. In late-type galaxies, the occurrence and the luminosity of bright HMXBs (see e.g., Grimm et al. 2003; Ranalli et al. 2003; Mineo et al. 2011) and of ULXs (e.g., Mapelli et al. 2009, 2010) are found to correlate with the SFR.

It was shown already with the XLF of the Cartwheel Galaxy (Wolter & Trinchieri 2004) and of NGC 2276 (Wolter et al. 2015) that the Grimm et al. (2003) relation linking the HMXB luminosity function with the SFR of the galaxy gives consistent results. Grimm et al. (2003) use 14 galaxies with a total of 99 sources above $L_X > 2 \times 10^{38}$ erg s^{-1} in the (2–10 keV) band.

Table 4
X-Ray Detected Sources in AM 0644-741, Arp 148, and Arp 143

Source #	Pos (FK5)		Counts	$f_X^{[0.5-10\,keV]}$ (a)	$L_X^{[0.5-10\,keV]}$ (b)	$L_X^{[2-10\,keV]}$ (b)	XLF Corr (c)	Notes
AM0644x1	06 42 58.62	−74 14 44.1	28.9 ± 5.5	7.95 ± 2.1	8.0	5.1	1.0	
AM0644x2	06 43 01.40	−74 15 16.1	46.3 ± 6.9	12.6 ± 2.8	12.6	8.1	1.0	
AM0644x3	06 43 02.27	−74 14 11.1	107.3 ± 10.4	28.5 ± 5.1	28.6	18.3	⋯	AGN in Heida et al. (2013)
AM0644x4	06 43 04.81	−74 13 43.1	36.4 ± 6.1	9.8 ± 2.7	9.8	6.3	1.0	
AM0644x5	06 43 06.08	−74 14 10.9	85.1 ± 9.3	22.3 ± 4.1	22.4	14.3	⋯	Nucleus
AM0644x6	06 43 06.51	−74 14 48.7	7.6 ± 2.8	2.1 ± 1.3	2.1	1.3	1.67	
AM0644x7	06 43 07.71	−74 15 02.1	8.4 ± 3.0	2.3 ± 1.5	2.3	1.4	1.33	
AM0644x8	06 43 10.54	−74 14 06.9	19.2 ± 4.5	5.1 ± 1.7	5.1	3.3	1.05	
AM0644x9	06 43 10.64	−74 14 34.9	31.4 ± 5.7	8.5 ± 2.2	8.5	5.4	1.0	
Gal	06 43 25.50	−74 15 26.2	30.41 ± 6.78	6.96 ± 2.6	7.0	4.44	⋯	Possible bullet? Few et al. (1982)
Arp148x1	11 3 52.35	+40 51 1.4	18.4 ± 4.4	3.5 ± 0.9	8.8	5.7	1.0	
Arp148x2	11 3 52.74	+40 50 51.3	14.8 ± 4.0	2.8 ± 0.9	7.1	4.6	1.0	
Arp148x3	11 3 53.99	+40 51 0.1	139.2 ± 11.9	25.8 ± 4.0	65.1	42.1	⋯	Nucleus/Galaxy
Star?	7 46 48.81	+39 02 01.7	28.7 ± 5.39	8.6 ± 2.8	⋯	⋯	⋯	Not related
Arp143x1	7 46 51.85	+39 00 50.6	21.8 ± 4.7	6.9 ± 2.6	2.7	1.7	1.0	
Arp143x2	7 46 52.04	+39 01 34.8	83.7 ± 9.2	25.0 ± 4.7	9.8	63	–	Bridge?
Arp143x3	7 46 52.97	+39 02 35.4	23.7 ± 4.9	7.3 ± 2.3	2.9	1.9	–	Not on ring (N2444)
Arp143x4	7 46 53.08	+39 01 54.9	16.5 ± 4.1	4.8 ± 1.9	1.9	1.2	–	Nucleus N2444
Arp143x5	7 46 53.20	+39 00 51.6	32.7 ± 5.7	9.6 ± 2.5	3.8	2.5	1.0	Radio source
Arp143x6	7 46 53.32	+39 00 38.8	7.9 ± 2.8	4.0 ± 2.4	1.6	1.0	1.25	
Arp143x7	7 46 53.38	+39 00 51.7	35.8 ± 6.0	10.9 ± 2.7	4.3	2.8	1.0	
Arp143x8	7 46 53.96	+39 00 27.5	11.8 ± 3.5	3.6 ± 1.8	1.4	0.9	1.10	
Arp143x9	7 46 53.97	+39 00 01.9	9.8 ± 3.2	3.1 ± 1.5	1.2	0.8	1.18	
Arp143x10	7 46 54.35	+39 02 40.6	669.6 ± 25.9	226.0 ± 14.0	2.8×10^5	1.8×10^5	⋯	Sy1 $z = 0.6155313$ (SDSS)
Arp143x11	7 46 55.14	+39 00 54.4	66.4 ± 8.2	19.2 ± 3.9	7.5	4.8	⋯	Nucleus N2445+radio source
Arp143x12	7 46 55.52	+39 00 19.5	10.7 ± 3.3	3.7 ± 1.7	1.4	0.9	1.10	
Arp143x13	7 46 55.68	+39 00 21.2	18.7 ± 4.4	5.6 ± 2.1	2.2	1.4	1.02	
Arp143x14	7 46 55.96	+38 59 56.0	12.8 ± 3.6	4.2 ± 2.0	1.6	1.0	1.09	

Notes. Fluxes (0.5–10.0 keV) are computed by CIAO/SRCFLUX assuming N_H as in Table 1 and $\Gamma = 1.7$. Quoted errors are all 90%.
[a] Unabsorbed flux in units of 10^{-15} erg cm^{-2} s^{-1}.
[b] Unabsorbed luminosity in units of 10^{39} erg s^{-1}.
[c] Multiplicative correction as derived from Kim & Fabbiano (2003).

The Grimm et al. (2003) function is normalized using the sum of the SFR values for the seven galaxies ($SFR_{Tot} = 43.5\ M_\odot\,yr^{-1}$, see Section 2.1). The luminosity is rescaled to our 0.5–10 keV band by using a power-law slope of $\Gamma = 1.7$. Given the uncertainties in SFR measures, we plot for reference the Grimm et al. (2003) function normalized to SFR = 35 $M_\odot$ yr^{-1} and SFR = 50 $M_\odot$ yr^{-1}, which represent a lower and an upper envelope for the XLF, respectively.

Mineo et al. (2012) selected a sample of 29 local galaxies ($D < 40$ Mpc) with SFR in the range 0.1–15 $M_\odot\,yr^{-1}$ to discuss the connection with recent star formation activity and binary evolution. They point out that a few incorrect assumptions have been used to derive the Grimm et al. (2003) functional form, however their relation between the SFR and the total L_X is very similar to Grimm et al. (2003). It is of interest here to verify the relation with the total luminosity of HMXBs, given in their Equation (22): L_X (erg s^{-1}) = 2.61×10^{39} (SFR/$M_\odot\,yr^{-1}$). The total luminosity of the sum of the detected point sources is definitely consistent with this estimate, although a similar scatter in the L_X versus SFR relation is evident. This could be due either to large uncertainties in the determination of the correct SFR or to some intrinsic physical effects.

A large sample of ULXs has been assembled by Swartz et al. (2011) by searching about a hundred galaxies, up to $D = 14.5$ Mpc. The total effective SFR is ∼50 $M_\odot\,yr^{-1}$, coincidentally very similar to the RiGs' value. We plot their XLF curve in Figure 5 for reference as a dashed line, after rescaling the luminosity to the 0.5–10 keV band by using a power-law slope of $\Gamma = 1.7$. The number of ULXs in the Swartz et al. (2011) sample is 86 (to be compared with our 50) at $L_X \geqslant 10^{39}$ erg s^{-1}; 16 (to be compared with our 23) at $L_X \geqslant 5 \times 10^{39}$ erg s^{-1}; and six (to be compared with our eight) at $L_X \geqslant 10^{40}$ erg s^{-1}. At face value, the RiG's XLF is flatter than the Swartz et al. one. However, a straightforward comparison would be incorrect, as we know that we have lost some sources at low fluxes. Figure 5 shows a more significant comparison between the distribution corrected for the presence of diffuse emission and the Swartz et al. (2011) fit. In comparison with the Grimm et al. (2003) curve, we see an excess of only two sources at high luminosities, indicating that a higher cut-off L_X might be more appropriate for the RiG XLF. The trend of RiG's XLF to be flatter with respect to Swartz et al. (2011) is still present, indicating a larger incidence of high L_X sources, consistent with the fact that the Swartz et al. (2011) sample includes galaxies of all types including ellipticals, and

Table 5
List of Sources from the Literature Used to Compute the XLF

Name	L_X^{orig} ($\times 10^{39}$ erg s^{-1})	L_X(0.5–10 keV) ($\times 10^{39}$ erg s^{-1})	Net Counts	XLF Corr[a]	Notes
Cart-N6	1.41	3.36	19.97 ± 4.69	1.0	(a, b)
Cart-N7	5.01	11.86	70.64 ± 8.60	1.0	Counts in 0.3–7 keV
Cart-N9	4.68	11.15	66.20 ± 8.31	1.0	
Cart-N10	27.54	65.49	383.77 ± 19.77	1.0	
Cart-N12	3.09	7.43	43.75 ± 6.78	1.0	
Cart-N13	2.69	6.37	38.02 ± 6.40	1.0	
Cart-N14	7.59	17.70	105.92 ± 10.54	1.0	
Cart-N15	1.15	2.66	16.06 ± 4.24	1.0	
Cart-N16	6.76	15.93	94.51 ± 9.90	1.0	
Cart-N17	8.32	19.47	116.10 ± 10.95	1.0	
Cart-N20	0.93	2.30	13.20 ± 3.87	1.0	
Cart-N21	0.50	1.19	6.97 ± 2.83	1.25	
Cart-N22	1.02	2.47	14.28 ± 4.00	1.0	
Cart-N23	0.60	1.45	8.54 ± 3.16	1.10	
Cart-N24	0.37	0.86	5.16 ± 2.45	1.68	
N922-2	0.68	0.69	8.92	1.19	(c)
N922-3	3.87	3.92	46.69	1.0	Counts corrected for PSF in 0.3–8 keV
N922-4	24.20	24.49	341.08	1.0	
N922-5	1.19	1.20	14.57	1.05	
N922-6	1.02	1.03	13.08	1.10	
N922-7	0.52	0.53	6.24	1.67	
N922-8	3.10	3.14	44.31	1.0	
N922-9	0.98	0.99	13.08	1.10	
N922-11	3.91	3.96	43.42	1.0	
N922-12	8.67	8.77	121.33	1.0	
N922-13	0.88	0.89	12.48	1.14	
N922-14	0.64	0.65	7.73	1.33	
Arp 147-Ring1	6.2	7.52	14.7 + 4.2 − 0.5	1.25	(d)
Arp 147-Ring2	2.7	3.39	6.7 + 3.0 − 2.3	2.5	Counts in 0.5–8 keV
Arp 147-Ring3	1.4	1.47	2.7 + 2.1 − 1.4	10	
Arp 147-Ring4	1.6	2.06	3.7 + 2.4 − 1.7	5	
Arp 147-Ring5	5.1	3.61	7.4 + 3.2 − 2.5	2.2	
Arp 147-Ring6	1.9	2.43	4.5 + 2.6 − 1.9	3.3	
Arp 147-Ring7	6.9	5.63	10.6 + 3.7 − 3.0	1.7	
Arp 147-Ring8	6.7	6.25	11.7 + 3.8 − 3.0	1.42	
Arp 147-Ring9	5.7	5.54	10.5 + 3.7 − 3.0	1.7	
Arp 284-4	64	64.1	2657 ± 52	1.0	(e, f)
Arp 284-5	0.5	0.5	21 ± 5	1.0	Counts in 0.3–8 keV
Arp 284-6	0.6	0.6	21 ± 5	1.0	
Arp 284-7	0.7	0.7	26 ± 5	1.0	
Arp 284-8	0.8	0.8	30 ± 6	1.0	
Arp 284-9	0.6	0.6	22 ± 5	1.0	
Arp 284-10	0.3	0.3	10 ± 3	1.05	
Arp 284-11	0.8	0.8	30 ± 6	1.0	
Arp 284-12	24	24.1	1076 ± 33	1.0	

Notes. This table reports the original published L_X and the unabsorbed L_X in the 0.5–10 keV band, computed assuming $\Gamma = 1.7$ and Galactic N_H as in Notes (and Table 1). (a) Originally published as Log L_X. (b) $N_H = 1.9 \times 10^{21}$ cm^{-2}. (c) $N_H = 1.6 \times 10^{20}$ cm^{-2}. (d) $N_H = 6.2 \times 10^{20}$ cm^{-2}. (e) Originally published in units of 10^{38} erg s^{-1}. (f) $N_H = 1.8 \times 10^{21}$ cm^{-2}.
[a] Multiplicative correction as derived from Kim & Fabbiano (2003).

therefore has a substantial population of low-mass X-ray binaries with a steeper XLF. We think that the outliers effect merits further investigation even though the small number statistics definitely affects the results.

4. Discussion

We have presented the first XLF derived solely from RiGs and, in particular, from sources associated to the ring itself. We deem this a "clean" sample of ULXs produced from a single burst of recent star formation in a peculiar and energetic environment.

There are additional X-ray sources in the galaxies' area, but their chance of being interlopers is larger than in the ring (see e.g., Wolter & Trinchieri 2004; Heida et al. 2013; Wolter et al. 2015), otherwise they could be due either to a different formation mechanism or to a different episode of star formation.

In late-type galaxies, there is a strong and almost linear correlation between the number of ULXs per host galaxy and

Table 6
Upper Limits in Flux for Each Observation and Relative Corresponding Luminosity at the Distance of the Individual Galaxies

Name	f_X (0.5–2 keV) (10^{-15} erg cm^{-2} s^{-1})	L_X (0.5–2 keV) (10^{39} erg cm^{-2})	Area$_{ring}$ ($''$)	Contamination (src/galaxy)
Cartwheel Galaxy	0.18	0.32	2478	0.43
NGC 922	0.80	0.20	3888	0.27
Arp 147	2.7	0.54	294	0.009
AM 0644−741	0.83	0.78	3010	0.20
Arp 143	1.2	0.44	2032	0.11
Arp 148	1.1	2.63	282	0.016
Arp 284	0.8	0.44	1399	0.10

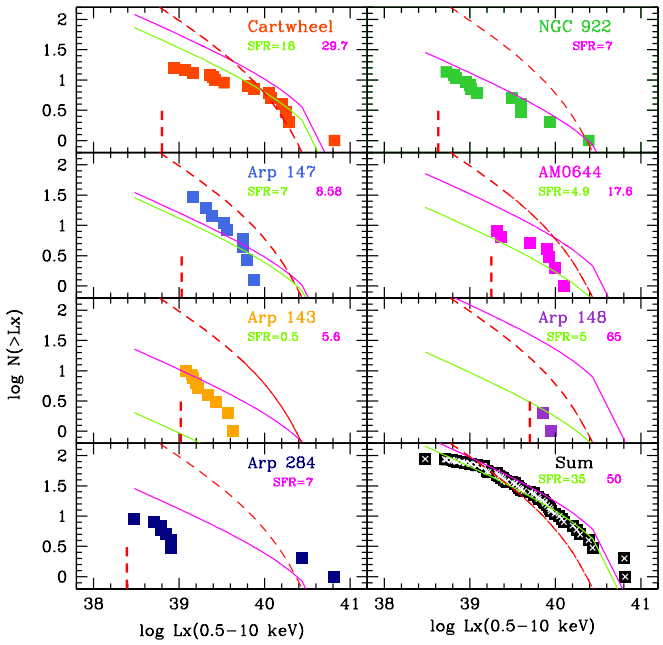

Figure 4. X-ray luminosity function (XLF) for the seven individual galaxies with upper limits (vertical dashed line) as in Table 6. The dashed red line is the model from Swartz et al. (2011). The pink and green solid lines are the models of Grimm et al. (2003), normalized to the SFR from Table 2 as indicated in the panels (see the text also). We stress that the uncertainty on the SFR measure is large, therefore the value for the single galaxy might not be representative.

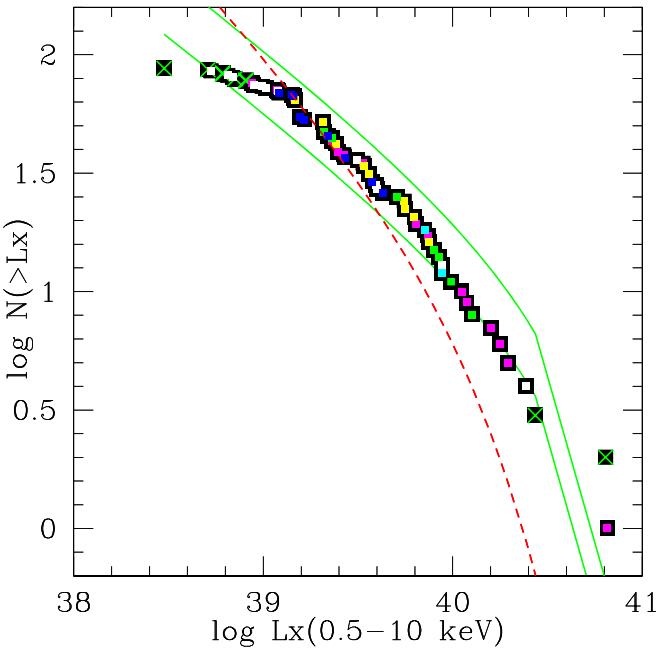

Figure 5. Total X-ray luminosity function (XLF) derived from the seven observed ring galaxies (see the text for details). The green line is the model of Grimm et al. (2003), normalized to SFR = 35 $M_\odot$ yr^{-1} (lower curve), and to 50 $M_\odot$ yr^{-1} (upper curve). The sum of the SFR for the 7 galaxies from Table 2 is 43.5 $M_\odot$ yr^{-1}. Sources with the same color are from the same galaxy. The dashed red line is the model from Swartz et al. (2011) that corresponds to an effective SFR = 50 $M_\odot$ yr^{-1} .

the SFR of the host galaxy (e.g., Mapelli et al. 2009, 2010, 2011; Swartz et al. 2009; Mineo et al. 2011). This has been interpreted as the smoking gun for the association of ULXs with high-mass X-ray binaries in regions of recent star formation. In Figure 6, we compare the galaxies considered in this paper with the sample of 66 late-type galaxies reported by Mapelli et al. (2011), which is an update of the sample published by Mapelli et al. (2010). Given the large uncertainty of the SFR we plot an error bar at 50% of the SFR value, for consistency with Mapelli et al. (2010). With the addition of the ring galaxies studied in this paper, the total correlation remains consistent with that reported by Mapelli et al. (2011). Moreover, our galaxies occupy the high SFR and high ULX number region of the plane covered by the comparison sample.

Several studies (Mapelli et al. 2009, 2010, 2011; Kaaret et al. 2011; Prestwich et al. 2013; Brorby et al. 2014, 2016) also suggest that there is an anti-correlation between the number of ULXs per host galaxy (normalized to the SFR) and the metallicity Z of the host galaxy. The interpretation of this result is still debated. This might indicate that a large fraction

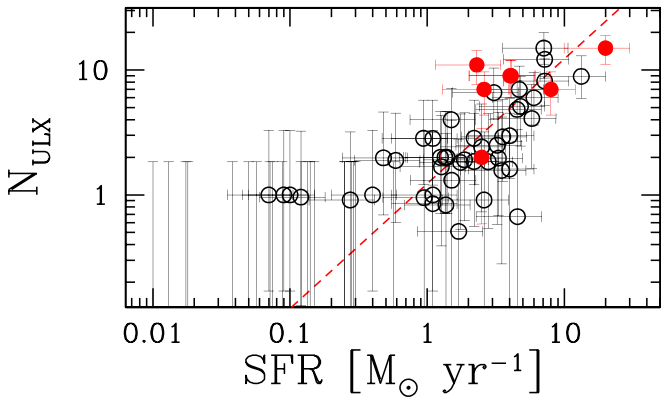

Figure 6. Number of ULXs per galaxy as a function of the host's SFR. Filled red circles are galaxies from this paper, while open black circles are from Mapelli et al. (2011). Error bars on the SFR are derived assuming a 50% uncertainty for all measures as in the previous papers. The red dashed line is the power-law fit obtained assuming that the index of the power law is equal to 1.

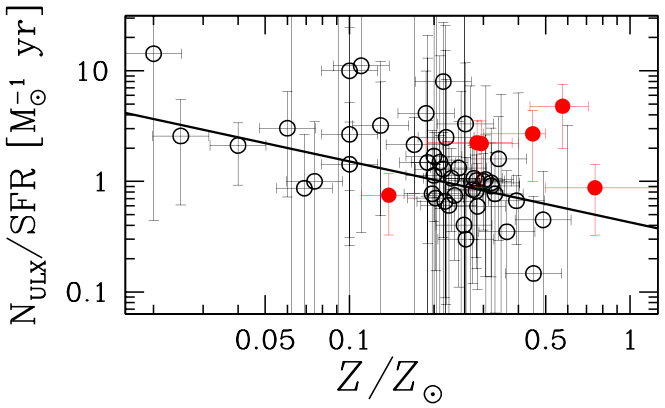

Figure 7. Number of ULXs per host galaxy, normalized to the SFR, vs. host's metallicity (Z). Filled red circles are galaxies from this paper, while open black circles are from Mapelli et al. (2011). We assume $Z_\odot = 0.02$. The solid black line is the power-law fit from Mapelli et al. (2011). Adding the new galaxies does not change the fit significantly with respect to Mapelli et al. (2011) (the power-law index changes from $-0.55^{+0.21}_{-0.19}$ to $-0.50^{+0.22}_{-0.21}$). The plotted uncertainties in the RiG values reflect the latitude of the measures. True uncertainties are most probably larger. Arp 148 is not shown because it lacks a metallicity measurement.

of ULXs are associated with massive stellar black holes (>20 $M_\odot$), which are expected to form at sub-solar metallicity (e.g., Mapelli et al. 2009, 2013; Zampieri & Roberts 2009; Mapelli & Zampieri 2014). Alternatively, it might suggest that metal-poor X-ray binaries are more luminous than their metal-rich peers (e.g., Linden et al. 2010), which could be the case for both BH or NS counterparts.

Figure 7 shows the number of ULXs (normalized to the SFR) versus the metallicity for six of the galaxies in our sample (Arp 148 is not included because it lacks a metallicity measurement), compared with the sample of Mapelli et al. (2011). The overall trend is still the same, and our RiGs seem to sit at the high $N_{\rm ULX}$ and high metallicity end. While this seems a tantalizing result, it is important to stress that most galaxies in our sample (with the exception of the Cartwheel) lack an accurate metallicity estimate, while the sample of Mapelli et al. (2011) was selected on the basis of the availability of a reliable metallicity estimate. We stress that the true uncertainties on the metallicity content is probably much higher than what plotted here, which reflects the maximum and minimum measure, or 0.1 dex, whichever is larger.

We investigate if the galaxy impact has a direct effect on the nuclear activity of the target galaxies. Most, but not all, of the RiGs show emission in the region corresponding to the original nucleus of the galaxy before the impact. In two galaxies, it is not straightforward to distinguish between the circumstellar diffuse emission of the galaxy and a central nuclear source (NGC 922), or it is not obvious where the optical nucleus currently is (Arp 147). The impact, in fact, might have been slightly different for different galaxies and/or projection effects might make the nucleus appear projected onto the ring (Gerber et al. 1992; Mapelli & Mayer 2012). The presence of an active nucleus is not ubiquitous: the Cartwheel Galaxy, for instance, does not have one. With the small statistics available, we infer about a 60% chance of finding an X-ray faint nucleus ($L_{\rm X} = 10^{39-40}$ erg s^{-1}) in RiGs implying that the effect of the impact on the activity of the nucleus, if present, is mild.

As discussed in Section 3, we find a substantial agreement with previous measures of the XLF (e.g., Swartz et al. 2011), with a hint to a flatter slope and a larger number of bright ULXs in RiGs. An interesting comparison could be made with the results of Wang et al. (2016) for more than 300 galaxies spanning all morphological types observed in the *Chandra* ACIS catalog. (Similar analyses were done previously, with smaller samples, by Kilgard et al. 2002, 2005.) These authors find a decrease in the steepness of the XLF going from early to late types, with peculiar and irregular being the flattest. The high L_X sample is dominated by late-type objects, which in turn is dominated by spirals. The peculiar galaxies slope, to which RiGs should better compare, is $\alpha = 0.55 \pm 0.30$, consistent with findings in this paper and in Swartz et al. (2011).

Given the recent discovery of PULXs (see Section 1), it is tempting to speculate about the composition of the XLF in this sample. We do not really know how to distinguish observationally PULXs, unless pulsation are seen, which might be a rare event also for known PULXs. A first attempt at proposing a discrimination has been based on the spectral shape of the X-ray emission (Pintore et al. 2017). In our case, however, the sources are too faint to measure the spectral shape of single sources. The spectrum of the collective sample of detected point sources has a slope of ~1.6–1.7, which does not allow us to discriminate. A bimodal flux distribution has been observed in a few PULXs, which might depend on the propeller effect (Tsygankov et al. 2016; Israel et al. 2017a, 2017b) or on changes in the accretion rate leading to accretion flow sphericization (Grebenev 2017). To establish the presence of a low flux state is a very observationally consuming task.

The collective sample of RiGs seems to confirm the effect of low metallicity on the production of ULXs, especially if compared with a sample of nearby Luminous Infrared Galaxies (Luangtip et al. 2015) selected to have a large SFR (>7 $M_\odot$ yr^{-1}) which shows a large deficit in ULX per unit SFR, consistent also with the results of the high metallicity sample from Prestwich et al. (2013). The luminous infrared galaxies in the Luangtip et al. (2015) sample have, in fact, metallicity generally $Z > Z_\odot$; however, the authors claim a significant contribution from dust which obscures the emission of the fainter sources and impedes their detection. The issue is possibly more complex and better and more adequate measures—e.g., metallicity at different position in the galaxy—are necessary to address it.

5. Conclusions

We have collected all the "bright and famous" ring galaxies observed by *Chandra* with the aim of studying their point sources population detected along the ring. We use both our analysis and the literature data to gather an homogeneous sample of 50 ULXs, while 63 sources in total are detected along the seven rings. We construct the first ring-only XLF. This is an estimate of the ULX luminosity distribution at a young age after the burst of star formation, even if uncertainties in the age of the stellar population are still large, both theoretically and observationally. However, the young age of the encounter favors both high-mass donors and BH accretor, as we should be observing these galaxies at most a few hundreds Myr after the beginning of the star formation episode (see e.g., Renaud et al. 2018). We see a larger average number of ULXs per galaxy than in other galaxies, even if there is not a statistical distinction with the bulk of spiral galaxies XLF. We are tempted to favor a high-mass BH interpretation for the brightest objects, given their relative higher luminosities, given also the recent discovery of BHs of mass in excess of 60 $M_\odot$

due to their gravitational wave emission from coalescence by the LIGO-Virgo collaboration (Abbott et al. 2016, 2017a, 2017b). RiGs, the Cartwheel in particular due to its large number of ULXs, are perfect testbeds for models of binary formation and the origin of ULX, such as the one from Wiktorowicz et al. (2017).

We thank Alberto Moretti, Doug Swartz, Grzegorz Wiktorowicz, and Andreas Zezas for useful discussions and input. We also thank the referee for useful comments that helped improve the paper. This research has made use of data obtained from the *Chandra* Data Archive and software provided by the *Chandra* X-ray Center (CXC) in the application packages DS9, CIAO, ChIPS, and Sherpa. The CXC is operated for NASA by the Smithsonian Astrophysical Observatory. Optical images were taken with the NASA/ESA *Hubble Space Telescope*, and obtained from the *Hubble* Heritage program and *Hubble* Legacy Archive, which is a collaboration between the Space Telescope Science Institute (STScI/NASA), the Space Telescope European Coordinating Facility (ST-ECF/ESA), and the Canadian Astronomy Data Centre (CADC/NRC/CSA). Funding for SDSS-III (we acknowledge here the use of one image) has been provided by the Alfred P. Sloan Foundation, the Participating Institutions, the National Science Foundation, and the U.S. Department of Energy Office of Science. This research has made use of the NASA/IPAC Extragalactic Database (NED), which is operated by the Jet Propulsion Laboratory, Caltech,under contract with NASA. A.W. acknowledges financial support from ASI through the ASI-INAF agreements 2015-023-R.0 and 2017-14-H.0. A.F. acknowledges support by the CXC under NASA contract NAS8-03060. M.M. acknowledges financial support from INAF through PRIN-SKA, "Opening a new era in pulsars and compact objects science with MeerKat" and from the MERAC Foundation through the project, "The physics of gas and protoplanetary discs in the Galactic centre."

Software: CIAO (Fruscione et al. 2006), Sherpa (Freeman et al. 2001; Doe et al. 2007), ChIPS, (Miller et al. 2015), DS9 (Joye 2011), XSPEC (Arnaud 1996), smongo https://www.astro.princeton.edu/~rhl/sm/.

References

Abbott, B. P., Abbott, R., Abbott, T. D., et al. 2016, PhRvD, 93, 122003
Abbott, B. P., Abbott, R., Abbott, T. D., et al. 2017a, PhRvL, 118, 221101
Abbott, B. P., Abbott, R., Abbott, T. D., et al. 2017b, PhRvL, 119, 141101
Abbott, B. P., Abbott, R., Abbott, T. D., et al. 2017c, PhRvD, 96, 022001
Abolfathi, B., Aguado, D. S., Aguilar, G., et al. 2018, ApJS, 235, 42
Anders, E., & Grevesse, N. 1989, GeCoA, 53, 197
Appleton, P. N., Ghigo, F. D., van Gorkom, J. H., Schombert, J. M., & Struck-Marcell, C. 1987, Natur, 330, 140
Appleton, P. N., & Marston, A. P. 1997, AJ, 113, 201
Arnaud, K. A. 1996, in ASP Conf. Ser. 101, Astronomical Data Analysis Software and Systems V, ed. G. H. Jacoby & J. Barnes (San Francisco, CA: ASP), 17
Athanassoula, E., & Bosma, A. 1985, ARA&A, 23, 147
Bachetti, M., Harrison, F. A., Walton, D. J., et al. 2014, Natur, 514, 202
Beirão, P., Appleton, P. N., Brandl, B. R., et al. 2009, ApJ, 693, 1650
Brorby, M., Kaaret, P., & Prestwich, A. 2014, MNRAS, 441, 2346
Brorby, M., Kaaret, P., Prestwich, A., & Mirabel, I. F. 2016, MNRAS, 457, 4081
Carpano, S., Haberl, F., Maitra, C., & Vasilopoulos, G. 2018, MNRAS, 476, L45
Crivellari, E., Wolter, A., & Trinchieri, G. 2009, A&A, 501, 445
Doe, S., Nguyen, D., Stawarz, C., et al. 2007, in ASP Conf. Ser. 376, Astronomical Data Analysis Software and Systems XVI, ed. R. A. Shaw, F. Hill, & D. J. Bell (San Francisco, CA: ASP), 543
Farrell, S. A., Webb, N. A., Barret, D., Godet, O., & Rodrigues, J. M. 2009, Natur, 460, 73
Feng, H., & Kaaret, P. 2008, ApJ, 675, 1067
Feng, H., Rao, F., & Kaaret, P. 2010, ApJL, 710, L137
Feng, H., & Soria, R. 2011, NewAR, 55, 166
Few, J. M. A., Arp, H. C., & Madore, B. F. 1982, MNRAS, 199, 633
Fogarty, L., Thatte, N., Tecza, M., et al. 2011, MNRAS, 417, 835
Fosbury, R. A. E., & Hawarden, T. G. 1977, MNRAS, 178, 473
Fragos, T., Lehmer, B. D., Naoz, S., Zezas, A., & Basu-Zych, A. 2013, ApJL, 776, L31
Freeman, P., Doe, S., & Siemiginowska, A. 2001, Proc. SPIE, 4477, 76
Fruscione, A., McDowell, J. C., Allen, G. E., et al. 2006, Proc. SPIE, 6270, 62701V
Fürst, F., Walton, D. J., Harrison, F. A., et al. 2016, ApJL, 831, L14
Gao, Y., Wang, Q. D., Appleton, P. N., & Lucas, R. A. 2003, ApJL, 596, L171
García-Vargas, M. L., González-Delgado, R. M., Pérez, E., et al. 1997, ApJ, 478, 112
Garmire, G. P., Bautz, M. W., Ford, P. G., Nousek, J. A., & Ricker, G. R., Jr. 2003, Proc. SPIE, 4851, 28
Gerber, R. A., Lamb, S. A., & Balsara, D. S. 1992, ApJL, 399, L51
Gerber, R. A., Lamb, S. A., & Balsara, D. S. 1996, MNRAS, 278, 345
Bogdán, Á., & Gilfanov, M. 2011, MNRAS, 418, 1901
Grebenev, S. A. 2017, AstL, 43, 464
Grimm, H.-J., Gilfanov, M., & Sunyaev, R. 2003, MNRAS, 339, 793
Heida, M., Jonker, P. G., Torres, M. A. P., et al. 2013, MNRAS, 433, 681
Higdon, J. L. 1995, ApJ, 455, 524
Higdon, J. L. 1996, ApJ, 467, 241
Higdon, J. L., Higdon, S. J. U., Martín Ruiz, S., & Rand, R. J. 2015, ApJL, 814, L1
Higdon, J. L., Higdon, S. J. U., & Rand, R. J. 2011, ApJ, 739, 97
Higdon, J. L., Rand, R. J., & Lord, S. D. 1997, ApJL, 489, L133
Higdon, J. L., & Wallin, J. F. 1997, ApJ, 474, 686
Israel, G. L., Belfiore, A., Stella, L., et al. 2017a, Sci, 355, 817
Israel, G. L., Papitto, A., Esposito, P., et al. 2017b, MNRAS, 466, L48
Jeske, N. A. 1986, PhD thesis, California Univ, http://adsabs.harvard.edu/abs/1986PhDT.....1J
Joye, W. 2011, in ASP Conf. Proc. 442, Astronomical Data Analysis Software and Systems XX, ed. I. N. Evans et al. (San Francisco, CA: ASP), 633
Kaaret, P., Feng, H., & Roberts, T. P. 2017, ARA&A, 55, 303
Kaaret, P., Schmitt, J., & Gorski, M. 2011, ApJ, 741, 10
Kilgard, R. E., Cowan, J. J., Garcia, M. R., et al. 2005, ApJS, 159, 214
Kilgard, R. E., Kaaret, P., Krauss, M. I., et al. 2002, ApJ, 573, 138
Kim, D.-W., & Fabbiano, G. 2003, ApJ, 586, 826
King, A., & Lasota, J.-P. 2016, MNRAS, 458, L10
Lançon, A., Goldader, J. D., Leitherer, C., & González Delgado, R. M. 2001, ApJ, 552, 150
Linden, T., Kalogera, V., Sepinsky, J. F., et al. 2010, ApJ, 725, 1984
Liu, J.-F., Bregman, J. N., Bai, Y., Justham, S., & Crowther, P. 2013, Natur, 503, 500
Luangtip, W., Roberts, T. P., Mineo, S., et al. 2015, MNRAS, 446, 470
Lynds, R., & Toomre, A. 1976, ApJ, 209, 382
Mapelli, M. 2016, MNRAS, 459, 3432
Mapelli, M., Colpi, M., & Zampieri, L. 2009, MNRAS, 395, L71
Mapelli, M., & Mayer, L. 2012, MNRAS, 420, 1158
Mapelli, M., Ripamonti, E., Zampieri, L., & Colpi, M. 2011, AN, 332, 414
Mapelli, M., Ripamonti, E., Zampieri, L., Colpi, M., & Bressan, A. 2010, MNRAS, 408, 234
Mapelli, M., & Zampieri, L. 2014, ApJ, 794, 7
Mapelli, M., Zampieri, L., Ripamonti, E., & Bressan, A. 2013, MNRAS, 429, 2298
Mayya, Y. D., Bizyaev, D., Romano, R., Garcia-Barreto, J. A., & Vorobyov, E. I. 2005, ApJL, 620, L35
Mesinger, A., Ferrara, A., & Spiegel, D. S. 2013, MNRAS, 431, 621
Mezcua, M., Roberts, T. P., Lobanov, A. P., & Sutton, A. D. 2015, MNRAS, 448, 1893
Miller, J., Burke, D. J., Evans, I. N., Evans, J. D., & McLaughlin, W. 2015, in ASP Conf. Proc. 495, Astronomical Data Analysis Software an Systems XXIV, ed. A. R. Taylor & E. Rosolowsky. (San Francisco, CA: ASP), 111
Mineo, S., Gilfanov, M., & Sunyaev, R. 2011, AN, 332, 349
Mineo, S., Gilfanov, M., & Sunyaev, R. 2012, MNRAS, 419, 2095
Moretti, A., Campana, S., Lazzati, D., & Tagliaferri, G. 2003, ApJ, 588, 696
Motch, C., Pakull, M. W., Soria, R., Grisé, F., & Pietrzyński, G. 2014, Natur, 514, 198

Pellerin, A., Meurer, G. R., Bekki, K., et al. 2010, AJ, 139, 1369
Pintore, F., Zampieri, L., Stella, L., et al. 2017, ApJ, 836, 113
Pizzolato, F., Wolter, A., & Trinchieri, G. 2010, MNRAS, 406, 1116
Portegies Zwart, S. F., Dewi, J., & Maccarone, T. 2004, MNRAS, 355, 413
Prestwich, A. H., Galache, J. L., Linden, T., et al. 2012, ApJ, 747, 150
Prestwich, A. H., Tsantaki, M., Zezas, A., et al. 2013, ApJ, 769, 92
Ranalli, P., Comastri, A., & Setti, G. 2003, A&A, 399, 39
Rappaport, S., Levine, A., Pooley, D., & Steinhorn, B. 2010, ApJ, 721, 1348
Renaud, F., Athanassoula, E., Amram, P., et al. 2018, MNRAS, 473, 585
Romano, R., Mayya, Y. D., & Vorobyov, E. I. 2008, AJ, 136, 1259
Schmitt, H. R., Calzetti, D., Armus, L., et al. 2006, ApJS, 164, 52
Smith, B. J., Struck, C., & Nowak, M. A. 2005, AJ, 129, 1350
Strauss, M. A., Huchra, J. P., Davis, M., et al. 1992, ApJS, 83, 29
Swartz, D. A., Soria, R., Tennant, A. F., & Yukita, M. 2011, ApJ, 741, 49
Swartz, D. A., Tennant, A. F., & Soria, R. 2009, ApJ, 703, 159
Tsygankov, S. S., Mushtukov, A. A., Suleimanov, V. F., & Poutanen, J. 2016, MNRAS, 457, 1101
van der Marel, R. P. 2004, in Coevolution of Black Holes and Galaxies, Vol. 1, ed. L. C. Ho (Cambridge: Cambridge Univ. Press), 37
Walton, D. J., Fürst, F., Harrison, F. A., et al. 2018, MNRAS, 473, 4360
Wang, S., Qiu, Y., Liu, J., & Bregman, J. N. 2016, ApJ, 829, 20
Wiktorowicz, G., Sobolewska, M., Lasota, J.-P., & Belczynski, K. 2017, ApJ, 846, 17
Wolter, A., Esposito, P., Mapelli, M., Pizzolato, F., & Ripamonti, E. 2015, MNRAS, 448, 781
Wolter, A., & Trinchieri, G. 2004, A&A, 426, 787
Wolter, A., Trinchieri, G., & Colpi, M. 2006, MNRAS, 373, 1627
Wolter, A., Trinchieri, G., & Iovino, A. 1999, A&A, 342, 41
Wong, O. I., Meurer, G. R., Bekki, K., et al. 2006, MNRAS, 370, 1607
Yue, B., Ferrara, A., Salvaterra, R., & Chen, X. 2013, MNRAS, 431, 383
Zampieri, L., & Roberts, T. P. 2009, MNRAS, 400, 677
Zezas, A., Fabbiano, G., Baldi, A., et al. 2007, ApJ, 661, 135